

Experimental and theoretical study on residual ultimate strength after impact of CF/PEEK-titanium hybrid laminates with nano-interfacial enhancement

Ji, C.; Hu, Jiqiang; Sadighi, M.; Alderliesten, R.C.; Wang, Bing; Sun, Yuguo

DOI

[10.1016/j.compscitech.2022.109871](https://doi.org/10.1016/j.compscitech.2022.109871)

Publication date

2022

Document Version

Final published version

Published in

Composites Science and Technology

Citation (APA)

Ji, C., Hu, J., Sadighi, M., Alderliesten, R. C., Wang, B., & Sun, Y. (2022). Experimental and theoretical study on residual ultimate strength after impact of CF/PEEK-titanium hybrid laminates with nano-interfacial enhancement. *Composites Science and Technology*, 232, Article 109871. <https://doi.org/10.1016/j.compscitech.2022.109871>

Important note

To cite this publication, please use the final published version (if applicable). Please check the document version above.

Copyright

Other than for strictly personal use, it is not permitted to download, forward or distribute the text or part of it, without the consent of the author(s) and/or copyright holder(s), unless the work is under an open content license such as Creative Commons.

Takedown policy

Please contact us and provide details if you believe this document breaches copyrights. We will remove access to the work immediately and investigate your claim.

Green Open Access added to TU Delft Institutional Repository

'You share, we take care!' - Taverne project

<https://www.openaccess.nl/en/you-share-we-take-care>

Otherwise as indicated in the copyright section: the publisher is the copyright holder of this work and the author uses the Dutch legislation to make this work public.



Experimental and theoretical study on residual ultimate strength after impact of CF/PEEK-titanium hybrid laminates with nano-interfacial enhancement

Chunming Ji^{a,b}, Jiqiang Hu^a, Mojtaba Sadighi^{b,c}, René Alderliesten^{b,**}, Bing Wang^{a,*}, Yuguo Sun^a

^a National Key Laboratory of Science and Technology on Advanced Composites in Special Environments, Harbin Institute of Technology, Harbin, 150001, PR China

^b Structural Integrity & Composites Group, Faculty of Aerospace Engineering, Delft University of Technology, Kluyverweg 1, 2629 HS, Delft, the Netherlands

^c Department of Mechanical Engineering, Amirkabir University of Technology, P.O.Box 15875-4413, Tehran, Iran

ARTICLE INFO

Keywords:

Fiber metal laminates
CNT network
Impact behavior
Residual tensile strength
Shell theory

ABSTRACT

Fiber metal laminates (FMLs) provide a reliable approach for achieving lightweight in high-speed aerospace vehicles. However, the weak interfacial properties between metals and composites could significantly affect the deformation and failure modes of FMLs. In this paper, the low-velocity impact responses and damage mechanisms of CF/PEEK-Ti hybrid laminates with nano-interfacial enhancement by multi-walled carbon nanotubes (CNTs) were characterized and analyzed. The post-impact residual tensile strengths (RTS) were investigated experimentally using quasi-static uniaxial tests combined with digital image correlation, and were evaluated theoretically by developing an analytical prediction model that considers the internal thermal stress and dent geometry. Results show that the initial delamination thresholds of force and displacement during impact can be effectively increased via interfacial enhancement of CNT network. By using a 5% decrease in RTS retention rate as a criterion for damage tolerance, a significant strength decrease starts to appear at 3 J for the sandblasted-only laminates, which is improved to 10 J for the laminates with nano-interfacial enhancement. The proposed unified constitutive model can yield an acceptable prediction for RTS and failure strain of the hybrid laminate after impact, providing a guidance for the structural design and engineering applications of FMLs.

1. Introduction

Fiber metal laminates (FMLs) integrating the merit of metal and fiber-reinforced plastic exhibit significant weight reduction compared to traditional metallic materials, that become one of the most potential structural candidates for aerospace and other transportation applications due to their high specific strength, excellent resistance to fatigue and impact [1–3]. In particular, the second generation of FMLs known as glass fiber reinforced aluminum alloy laminate (GLARE) is incorporated in the largest commercial aircraft A380 with an area of nearly 380 m², which achieves a reduction of 794 kg in weight (10% lower density than aluminum alloy) [4,5]. Nevertheless, it has limited temperature resistance and cannot be employed for a long duration in supersonic vehicles with a surface temperature exceeding 177° [6]. Therefore, titanium-based FMLs using carbon fiber reinforced thermoplastics,

typically Polyimide (PI) and Polyether-ether-ketone (PEEK) [7,8], have been designed to meet such extreme operating environments for weight saving, while the application of titanium alloys eliminates the electrochemical corrosion issue between carbon fibers and aluminum alloys [9]. However, there is still a lack of systematic theoretical research work on interface strengthening and mechanical damage, which seriously restricts the application of titanium-based FMLs.

As a connection between the metallic and fiber-reinforced plastic layers, the microstructure and adhesive strength of the interface directly affect the internal stress transfer and damage accumulation mechanism in FMLs [10–12]. Besides, as a kind of laminated composites, FMLs are subject to significant residual stresses at the interface due to the difference in thermal expansion coefficients of components, which are prone to yield interfacial delamination under external damage, leading to a deterioration of structural properties [13–15]. Li et al. [16] examined

* Corresponding author.

** Corresponding author.

E-mail addresses: R.C.Alderliesten@tudelft.nl (R. Alderliesten), wangbing86@hit.edu.cn (B. Wang).

the effect of residual stress introduced by shot peening on the mechanical properties of FMLs and found that the compressive stress induced by shot peening increased the overall tensile strength. Hausmann et al. [17] adopted the finite element analysis and analytical models to predict the thermal residual stresses in FMLs, and several methods were summarized that are beneficial for reducing the thermal residual stresses, including (a) by post-stretching of metal layers [18], (b) by thermal post-treatments of FMLs, (c) by adjusting the composite lay-up. Additionally, to ensure the reliability during service, it is necessary to understand the influence of external damage as impact on the performance of titanium-based FMLs with different interfacial adhesion. To address this issue, Shanmugam et al. [19] investigated the low-velocity impact (LVI) performance of FMLs hybrid with ultra-high molecular weight polyethylene fibers under different Ti–6Al–4V surface treatments, the results showed that the crack of titanium layer on the non-impacted side plays an important role in absorbing the impact energy and that the enhancement of the interfacial properties can inhibit the crack growth. Lin et al. [20] studied the LVI response of GLARE laminates with two different surface treatments (anodization and plasma treatment) of aluminum and found that a larger bending deformation appeared due to the poor interfacial adhesion of the anodizing cases. Li et al. [21] characterized the impact behavior of titanium-based FMLs with different surface treatments of titanium, it was found that the improved interfacial strength yielded a low energy absorption capacity. Jakubczak et al. [22,23] compared experimentally the LVI behavior of conventional CFRP, aluminum-based, and titanium-based FMLs under different energies, they observed that the impact resistance of titanium-based FMLs is at least two times greater than that of aluminum-based and six times higher than that of conventional CFRP. However, there are limited studies that have investigated on the strengthening of interfacial adhesion and its related intrinsic mechanisms on the impact resistance of titanium-based hybrid laminates.

In the design and certification of damage tolerance, it is crucial to evaluate the effect of impact damage on the residual ultimate strength of the laminates [24]. Cortés and Cantwell [25] developed an analytical model for predicting the tensile modulus and strength of CF/PEEK-titanium hybrid laminates with different fiber orientations based on classical laminate theory, which was able to predict the initial failure under tensile loading well over a wide range of fiber orientations. Dadej et al. [26] established an isostrain elastoplastic model considering thermal stress to predict the static strength and fatigue life of aluminum-based FMLs with a hybrid of carbon and glass fibers, the prediction results showed a good agreement with the experiments. Sharma and Velmurugan [27] investigated the stress-strain behavior of titanium-based FMLs with different layup structures through experiments and classical laminate theory, it was found that the initial modulus of the laminate was not affected by the stacking structures, but the response after ultimate load was influenced. Christian et al. [28] employed the strain field that is obtained from digital image correlation (DIC) to predict the post-impact residual strength of carbon fiber composites and revealed that the strain-based assessment had a more reliable result compared to the ultrasonic technique. Nevertheless, the residual mechanical behaviors of titanium-based hybrid laminate have not been fully examined, and the theoretical studies in this field are still essential to meet the needs of engineering applications.

In this study, to improve the damage tolerance of CF/PEEK-titanium hybrid laminate, an easily-handled and effective surface treatment of titanium by depositing multi-walled carbon nanotubes (CNTs) [29] was adopted to enhance the interfacial adhesion. Subsequently, the LVI responses and damage mechanisms of the hybrid laminates with two different interfacial behaviors were investigated, the role of the deposited CNT network structure in energy absorption and improving the damage tolerance was discussed. Furthermore, the post-impact residual tensile strength (RTS) of the laminate was analyzed experimentally, the effect of the enhanced interfacial adhesion on RTS at different impact energy levels was discussed by axial strain distribution and failure

morphology. Finally, a thermo-mechanical constitutive model of CF/PEEK-titanium hybrid laminate after impact considering internal thermal stress and dent geometry was proposed and verified by experimental results.

2. Materials and methods

2.1. Materials

The CF/PEEK-titanium hybrid laminate examined in this research was composed of the commercially pure titanium sheet of TA2 (0.3 mm in thickness, purchased from Baoji titanium industry Co. Ltd.) and the unidirectional prepreg of CETEX TC1200 (0.13–0.14 mm in thickness, supplied by Ten Cate Co. Ltd.) based on carbon fibers AS-4 and thermoplastic polymer PEEK (59% in fiber volume fraction). A 0.1 mm-thick PEEK film sourced from Victrex plc. was placed between the titanium and CF/PEEK layers to provide a basic interfacial adhesion. Multi-walled CNTs with carboxyl functional groups (2–5 nm in inner diameter, 5–15 nm in outer diameter, 10–30 μm in length) were purchased from Chengdu Organic Chemicals Co. Ltd. The aluminum ions for carrying CNTs in the electrophoretic deposition (EPD) were derived from Aluminum nitrate nonahydrate ($\text{Al}(\text{NO}_3)_3 \cdot 9\text{H}_2\text{O}$, 99.99%), which was supplied by Aladdin Chemistry Co. Ltd. Table 1 lists the thermal and mechanical properties of the principal components in the hybrid laminate.

2.2. Preparation of CF/PEEK-titanium hybrid laminate

Prior to the preparation of the CF/PEEK hybrid laminate, surface pretreatment of the titanium layers is essential to achieve a basic adhesive behavior with PEEK. Two types of surface treatment methods for titanium were adopted in this study, including sandblasting and sandblasting followed by EPD of CNTs on the surface of titanium plates, of which the latter has been verified in the literature [29] to have an excellent strengthening effect on the short beam shear behavior of CF/PEEK-Ti hybrid laminate. The two types of specimens were recorded as sandblasted-only and CNT-enhanced laminates, respectively. With regard to the specific parameters of treatment, firstly, the titanium sheets were sandblasted with 80 μm brown corundum sand at a pressure of 0.2 MPa to prevent distortion, the spraying distance, angle, and time were set up as 100–150 mm, 90°, and 20 s, respectively. After sandblasting, the titanium sheets were separately washed with acetone in an ultrasonic cleaner for 5 min to remove any remaining sand and contamination. Subsequently, CNTs were electrophoretically deposited on the surface of the sandblasted titanium sheets. The electrophoretic solution was a well-dispersed CNTs suspension of acetone and ethanol at a volume ratio of 1:1, which has the CNTs concentration of 0.75 mg/mL and dispersed by an ultrasonic homogenizer (JY98-IIIDN, Ningbo Xinzhi Biological Technology Co., Ltd.). Aluminum nitrate nonahydrate was added to the solution in a mass ratio of 1:1 with CNTs, the spacing between the anode of the stainless steel plate and the cathode of the titanium sheet was fixed at 50 mm, then the deposition was carried out using a regulated DC power supply (APS3005S, ATTEN instrument) at a voltage of 30 V for 90 s. Finally, the titanium sheets with the deposited CNTs were dried at 100 °C for 10 min. The micromorphology of titanium subjected to different surface treatment methods is shown in Fig. 1.

After the surface pretreatment of titanium sheets, the hot-pressing method was employed to prepare the hybrid laminates with an orthogonal stacking sequence of Ti/[90/90/0/0]/Ti/[0/0/90/90]/Ti in a customized frame mold, where the rolling direction of titanium layers within the different layers was consistent. The stacking sequence referred to the commercially available GLARE 3 grade [18], but the plies were doubled to maintain a high fiber volume content (a PEEK film was added between titanium and CF/PEEK layers). The hot-pressing process started from ambient temperature to 390 °C at a heating rate of 3 °C/min. During this stage, a pressure of 0.2 MPa is simultaneously

Table 1
Thermal and mechanical properties of the principal components.

Materials	E_{11} (MPa)	E_{22} (MPa)	ν_{12}	ν_{21}	G_{12} (MPa)	α_1 ($10^{-6}/^{\circ}\text{C}$)	α_2 ($10^{-6}/^{\circ}\text{C}$)	σ_T (MPa)
TA2	114100	114100	0.33	0.33	46314	8.41 [30]	8.41	446.88
CF/PEEK	130000	10000	0.33	0.025	5200	-0.2	29	2280
PEEK	3660	3660	0.4	0.4	1300	47	47	97 ^a

^a Tensile strength at yield.

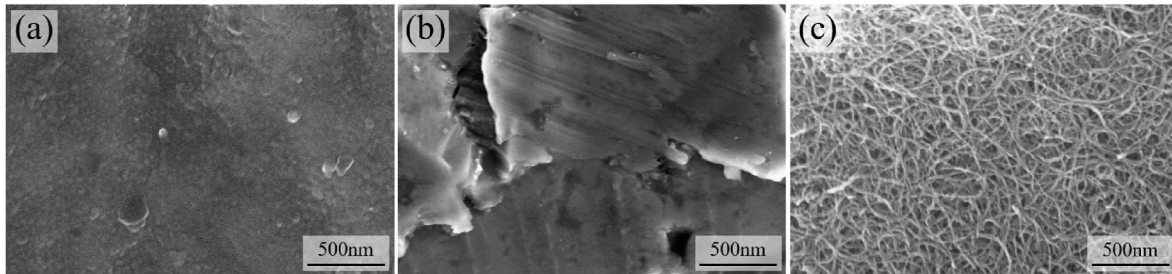


Fig. 1. Micromorphology of titanium subjected to different surface treatment methods [29]: (a) as-received; (b) after sandblasting and (c) after sandblasting and depositing CNTs.

applied to achieve effective heat transfer. Next, after the temperature reached 390°C , the pressure was increased to 1.6 MPa while holding for 30 min to ensure complete wetting of PEEK on the surface of the titanium. Finally, the laminate was air-cooled to ambient temperature with maintaining the pressure.

2.3. Experimental methods and characterization

The impact tests were conducted at room temperature using a drop-weight testing machine (CEAST 9350, Instron) as shown in Fig. 2. A pneumatic steel ring with an inner diameter of 40 mm was used to clamp the specimens to avoid movement during the impact. A hemispherical impactor with a diameter of 16 mm and a weight of 5.482 kg was employed for all impact tests. Impact energy levels of 3, 5, 10, 15, 20, 25, and 30 J (correspond to the impact velocities of 1.05, 1.35, 1.91, 2.34, 2.70, 3.02 and 3.31 m/s, respectively) were adopted to evaluate the impact failure mechanism of hybrid laminate. The geometry of the specimens prepared by water cutting was $75\text{ mm} \times 200\text{ mm}$, which was designed to be sized for the impact and tensile tests as shown in Fig. 2. The depth of dent was tactile measured by a mechanical digital depth indicator with an accuracy of 0.001 mm.

For determining the RTS of all sandblasted-only and CNT-enhanced specimens with initial impact damage, the tensile after impact tests were carried out using the MTS hydraulic testing machine with a maximum loading capacity of 500 kN, the loading was in displacement control with a rate of 2 mm/min. Both ends of the laminate were bonded with 2 mm-thick aluminum alloy tabs as shown in Fig. 2 to prevent premature failure and gripping issues according to ASTM D3039. Meanwhile, the global strains and displacements on the impacted surface of the laminates were captured using a 3D DIC system (Correlated Solutions, Inc.) with two cameras. Four samples for each impact and tensile condition were tested. The failure morphology on the hybrid laminate was examined by using a scanning electron microscope (SU8010, Hitachi) operated at 10 kV, and the cross-sectional fracture morphology was analyzed by using a stereomicroscope (SZ61, Olympus).

3. Test results and discussion

3.1. Impact responses at different impact energy levels

For the two types of hybrid laminates with different interfacial

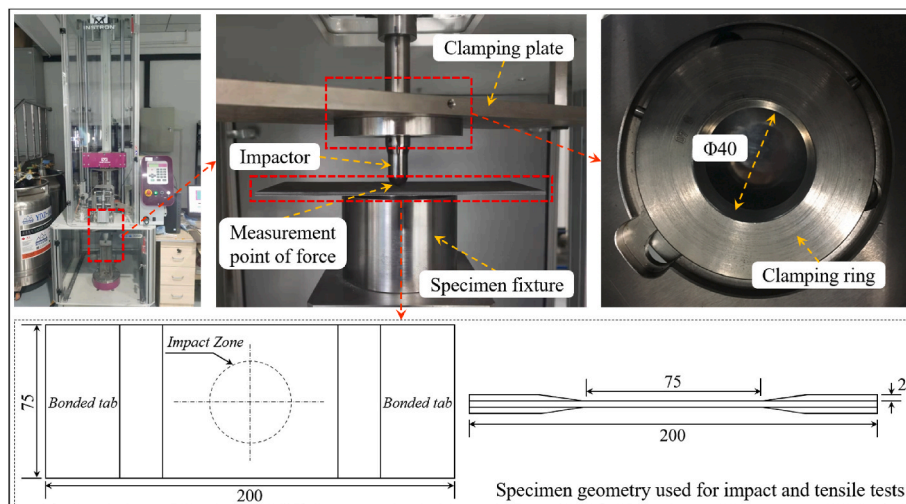


Fig. 2. Experimental set-up of impact tests and the specimen geometry used for impact and tensile tests.

enhancements, as presented in Fig. 3(a) and (b), a proportional scaling effect is shown in the force history as the impact energy varies. By comparing the force-displacement responses at different impact energy levels, it is observed that in the sandblasted-only cases, the average force at the first significant sudden drop point is about 3700 N, which corresponds to the first delamination failure of the laminate [31], while the deflection of specimen is approximately 1.07 mm. Moreover, with the increase of impact energy, the load undergoes several sharp drops, and the second significant sudden drop in force that first appears in 10 J corresponds to the cracking of titanium layer on the non-impacted side, which can be corroborated in Section 3.2. Besides, it should be noted that the remaining drops or fluctuations in force (after the two significant sudden drops in force) correspond to matrix cracking, fiber fracture, or other forms of delamination damage. For CNT-enhanced specimens, it can be seen from Fig. 3(b) that the general trend of the force-displacement curve is similar to that of the sandblasted-only specimen, but its average delamination threshold of force and deflection under impact loading are about 4300 N and 1.25 mm, respectively, which present a significant improvement greater than 15% compared to the sandblasted-only cases, indicating that the improved interlaminar adhesion behavior of the hybrid laminate is obtained due to the presence of CNT networks. The difference can be verified by a two-sample *t*-test, all of the *p*-values between the sandblasted-only and CNT-enhanced specimens at the same impact energy level are below the significance level of 0.05 as shown in Fig. 3(c). A noticeable fluctuation in force is observed in the force-displacement curves of CNT-enhanced specimens, which can be attributed to the occurrence of a massive pull-out of CNTs

due to delamination propagation, a similar result was also found in Ref. [32].

Furthermore, the force-displacement curves of the two types of specimens at the impact energy levels of 3 J and 20 J are compared. As shown in Fig. 4(a), there is no apparent sudden force drop in the loading phase, indicating that 3 J does not exceed the maximum impact energy which can induce delamination of the hybrid laminate, the kinetic energy is more absorbed by the elastic and plastic deformation of the titanium layers and friction between the sample surface and the impactor. For impact energy of 20 J as shown in Fig. 4(c), the initial delamination threshold of CNT-enhanced specimen in force is about 556 N higher than that of the sandblasted-only case, which has an improvement of 15.1%, demonstrating that the CNT networks could significantly increase the energy required for delamination and the damage tolerance of the hybrid laminate. The impact history for 20 J can be divided into three stages as shown in Fig. 4(d). In the first stage, the laminate absorbs energy mainly through elastic and plastic deformation of the titanium layers, there is no obvious damage in the composite layers and the specimen maintains a high stiffness. The second stage starts with the preliminary delamination between the non-impacted side of titanium layer and its adjacent CF/PEEK layer. As the impact energy increases, damage such as delamination propagation, matrix cracking, and fiber fracture are formed successively, then leading to a decrease in the stiffness of the laminate. The last stage relates to the rebound phase, where the impact energy reaches its maximum and the impactor starts to rebound until it is separated from the specimen, partial impact energy is converted into the rebound kinetic energy released by the impactor.

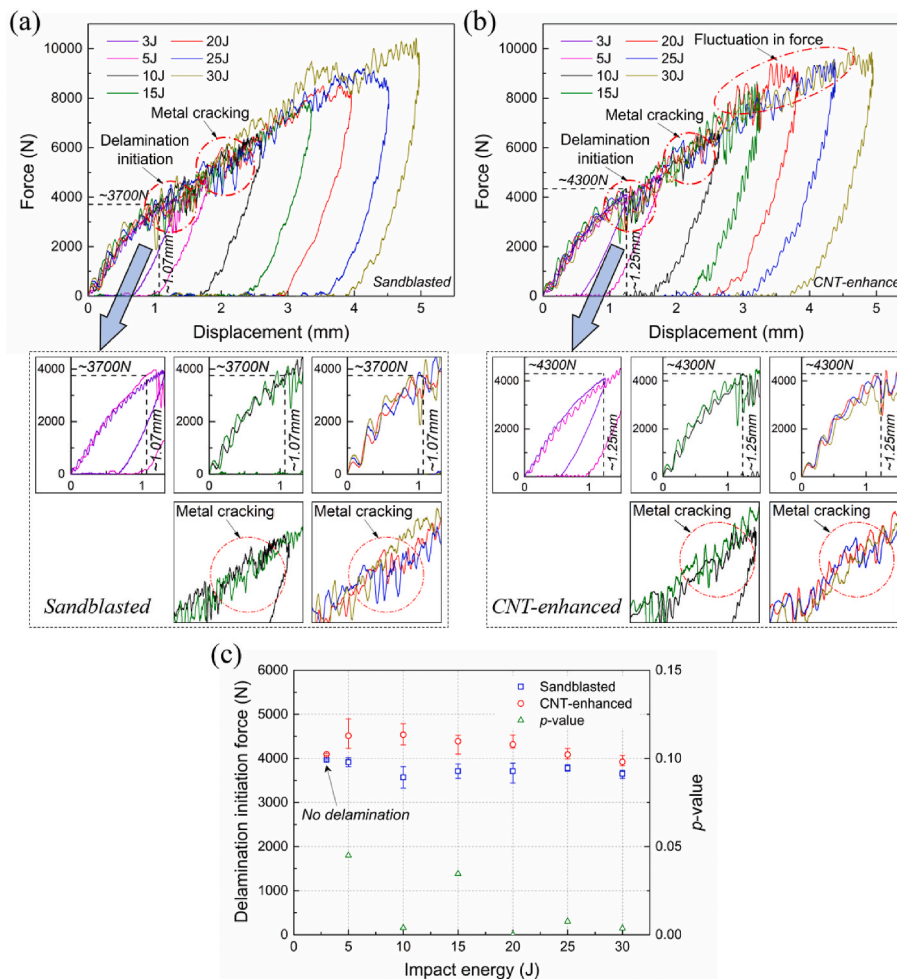


Fig. 3. Force-displacement curves of (a) sandblasted-only and (b) CNT-enhanced specimens at different impact energy levels; (c) comparison of delamination initiation forces and *p*-values at different impact energy levels.

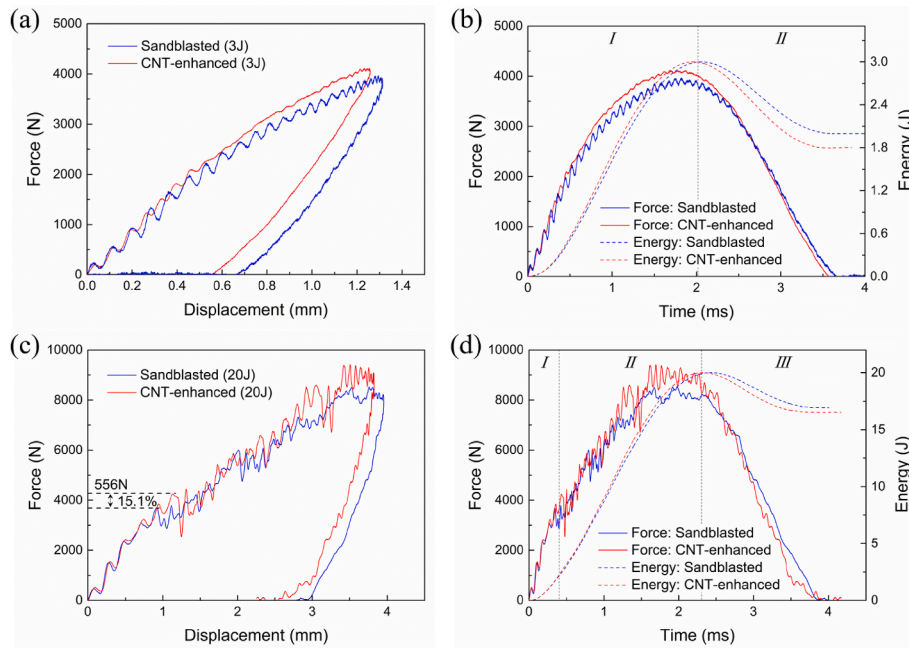


Fig. 4. Force-displacement curves at impact energy level of (a) 3 J and (c) 20 J; force-time and energy-time curves at impact energy level of (b) 3 J and (d) 20 J.

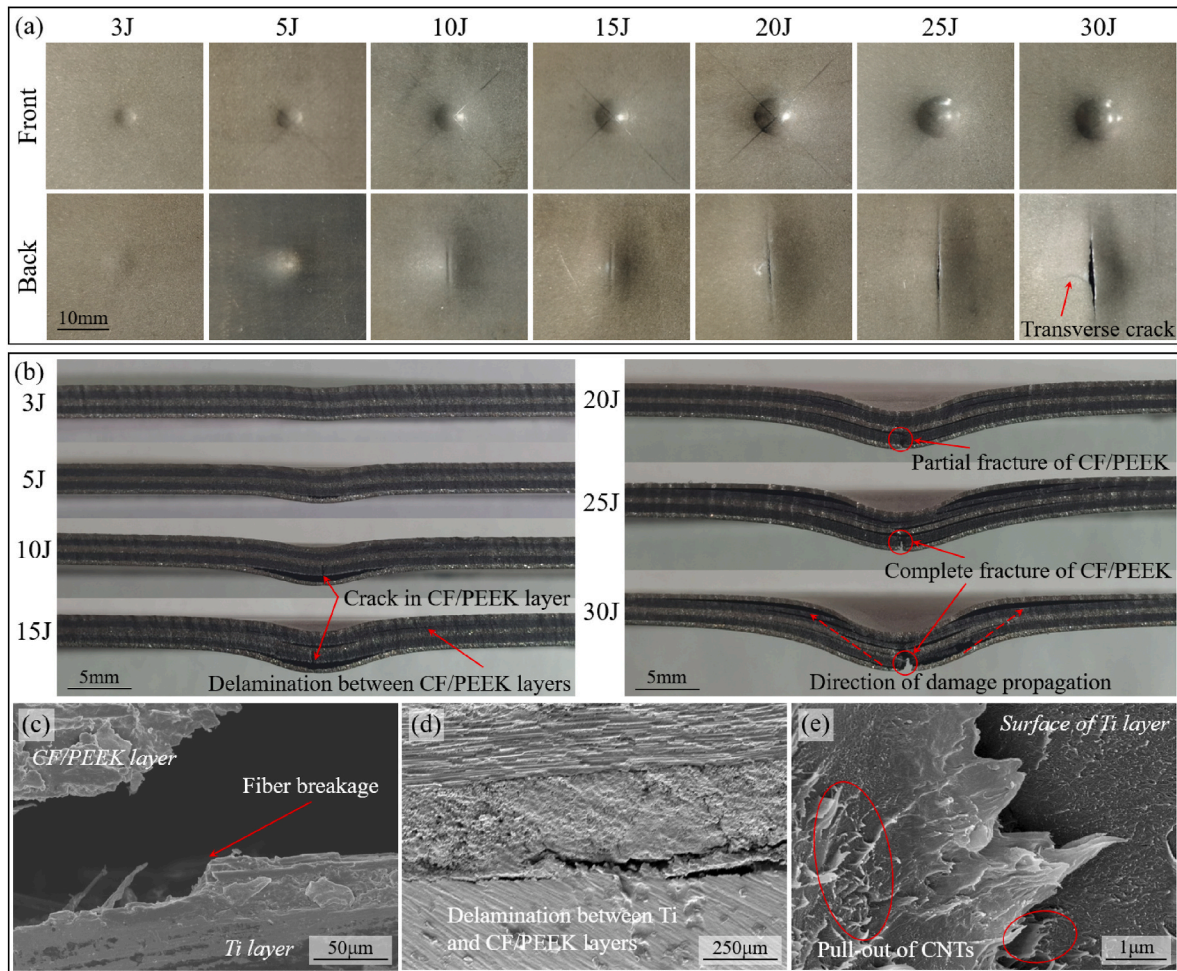


Fig. 5. Damage assessment of CNT-enhanced specimens subjected to various impact energy levels: (a) failure modes of impacted and non-impacted area; (b) cross-sectional views; (c-e) localized microscopic failure morphology at impact energy level of 15 J.

Compared to the sandblasted-only specimens, the contact force in the CNT-enhanced specimen also shows a phenomenon of fluctuation during the rebound stage, which could be attributed to the mismatch between the deformation of the titanium and CF/PEEK layers. The permanent deformation of the titanium layer due to plasticity leads to the delamination and propagation between the titanium and CF/PEEK layers during the rebound stage, which in turn causes the CNTs to be pulled out, resulting in a force fluctuation. Since there is no delamination of the hybrid laminate after 3 J impact, the impact history has only two stages as presented in Fig. 4(b).

3.2. Damage assessment after impact

The sandblasted-only and CNT-enhanced specimens have similar characteristics in macroscopic failure modes without significant differences. Fig. 5(a) exhibits the macroscopic failure modes of the impacted area on CNT-enhanced specimens subjected to various impact energy levels. The size of the front dent including diameter and depth gradually enlarges as the impact energy increases, and no obvious damage such as metal cracking appears in the front view. Meanwhile, no visible crack appears on the backside at impact energy levels of 3 J and 5 J. Starting from 10 J, the crack could be observed in the same direction as the outermost carbon fibers on the non-impacted side and its length gradually increases with increasing impact energy. Besides, a crack perpendicular to the direction of the adjacent composite layer is found on the back of the specimen at 30 J, indicating the fracture of carbon fibers within the CF/PEEK layers.

Furthermore, it can be seen from Fig. 5(b) that the delamination damage between the outer titanium and CF/PEEK layers on the non-impacted side comes first, which is induced by the deformation mismatch between the two during the rebound stage as mentioned above. At the impact energy levels of 10 J and 15 J, the cracks within the bottom CF/PEEK layers and the delamination between the middle titanium and CF/PEEK layers appear sequentially. As the impact energy increases (>20 J), the crack on the non-impacted side of the specimen is transited from the titanium layer to the CF/PEEK layer until complete fracture of the CF/PEEK layer appears (30 J). In addition, the delamination can also be found on both sides of the dent at 25 J and 30 J, as well as the delamination within the CF/PEEK layers. Therefore, it can be concluded that during impact loading, the damage sequence of the specimen is firstly delamination between the titanium and CF/PEEK layers on the non-impacted side, then cracking from the backside, finally delamination between the titanium and CF/PEEK layers on the impacted side.

The difference between the sandblasted-only and CNT-enhanced specimens is obvious in terms of the intra-layer microstructure, for the sandblasted-only cases, there is almost no residue of PEEK on the bonded surface of the titanium layer. In contrast, it can be observed from Fig. 5(c) that there are fractured fibers and a large amount of resin remaining at the delamination for the impact energy level of 15 J, which proves

that the CNT network structure enhances the interlayer bonding performance of the hybrid laminate. Meanwhile, the deposited network structure could lock PEEK firmly on the bonded surface of the titanium layers, preventing cracks from expanding along the metal-composite interface, as strongly evidenced in Fig. 5(d). In addition, the pull-out of CNTs on the delaminated surface of titanium layer can be observed in Fig. 5(e), indicating that the CNTs exhibit a bridging effect between the titanium and CF/PEEK layers, which reduces the delamination area and then plays a role in maintaining the residual mechanical properties of the hybrid laminate.

3.3. Mechanism of energy conversion

The global dent depth is the most intuitive way to quantify impact damage. As shown in Fig. 6(a), an approximately linear relationship between global dent depth and impact energy can be observed for the CF/PEEK-Ti hybrid laminate, which is different from the phenomenon of 'knee point' that could be commonly found in carbon fiber-reinforced polymer composites [33]. Besides, the sandblasted-only specimens have larger dent depth than that of CNT-enhanced cases at the same impact energy, implying that CNT network structure has further improved the impact resistance of the laminate and reduced the maximum deformation while inhibiting the delamination between the titanium and CF/PEEK layers. In other words, a higher impact energy is required for the CNT-enhanced specimens to induce the same maximum permanent deformation. Furthermore, the energy absorption ratio, defined as the ratio of absorbed energy to impact energy, is also considered to be a reliable indicator in evaluating impact damage [34]. From Fig. 6(b), it can be seen that the energy absorption ratio of the sandblasted-only specimen is higher than that of the CNT-enhanced case at the same impact energy level, which is attributed to the beneficial effect of the CNTs network structure in suppressing the deformation and delamination of the hybrid laminate while reducing the internal damage. Combined with Fig. 5(b), the energy absorption mechanism of the hybrid laminates corresponding to different impact energy levels can be mainly divided into four regions, which are elastic and plastic region, delamination region, matrix and metal cracking region, and fiber failure region. For all impact energy levels, elasto-plastic deformation dissipation is the dominant energy conversion mode, which has a value of energy absorption ratio exceeding 50% and no more than 70% from Fig. 6(b) (the specimen undergoes only elasto-plastic deformation at the impact energy level of 3 J, and does not enter the delamination region). The growth of energy absorption ratio slows down beyond 20 J. At the impact energy levels of 25 J and 30 J, the differences in average energy absorption ratio are significant, with 5.9% and 4.3% higher for sandblasted-only cases than CNT-enhanced cases, respectively.

3.4. Residual tensile strength after impact

For the non-impacted cases of both types of specimens as shown in

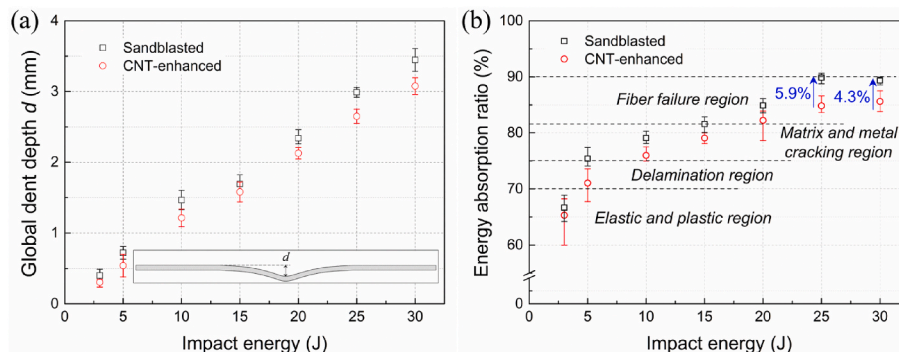


Fig. 6. For different impact energy levels: (a) global dent depth; (b) energy absorption ratio.

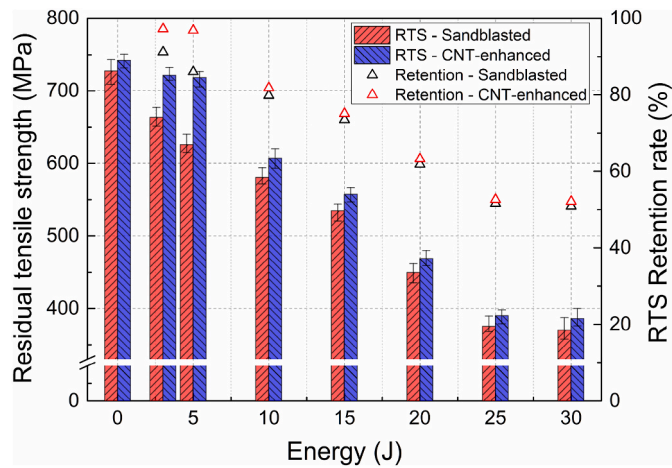


Fig. 7. RTS and RTS retention rate at different impact energy levels.

Fig. 7, the difference in ultimate tensile strength is limited, which means that the contribution of the randomly distributed CNT network structure to the tensile properties is weak, thus there is only a slight increase in the average tensile strength of CNT-enhanced specimens with the reference to sandblasted cases. For impacted specimens, the RTS of both types decreases gradually with the increase of impact energy. At the impact energy levels of 3 J and 5 J, there is a large difference in the RTS between the two types of specimens. In particular, the relatively low impact energy of 3 J causes a significant reduction in RTS of sandblasted-only specimens. The difference in RTS between the two types increases and reaches 14.8% at 5 J, where the CNT-enhanced specimens could still maintain more than 95% of the ultimate strength in the non-impacted case, while only 86% remains for the sandblasted-only specimens, indicating that the damage tolerance, as well as the impact resistance of the hybrid laminate, are improved after interfacial reinforcement by CNTs. In combination with the results of the global dent depth in Fig. 6 (a), the CNT-enhanced specimens exhibit a shallower dent depth compared with the sandblasted-only cases, which is one of the reasons for their higher RTS. However, the influence of dent geometry on RTS is significant when the dent depth is smaller than the half thickness of the laminate (about 1.2 mm), while for deeper dent depths (>1.2 mm), the effect of dent depth is not obvious and the RTS is mainly determined by the internal cracking state of the specimen.

A parameter, the RTS retention rate (the ratio of the RTS of impacted specimen to the tensile strength of non-impacted specimen), can be considered as a criterion for damage tolerance [35]. Taking the RTS retention rate of 95% as the threshold, it can be observed from Fig. 7 that for the sandblasted-only cases, a significant strength reduction starts at 3 J, which is 10 J for CNT-enhanced specimens, indicating that the CNT-enhanced specimens have a higher damage tolerance. Besides, at impact energy levels above 25 J, the RTS hardly changes with impact

energy for both types of specimens, since the damage (such as fiber breakage and metal cracking) to the laminate caused by the impact as shown in Fig. 5 is so severe that the dented area almost loses its load-bearing capacity. For impact energy of 30 J, the RTS retention rates are 50.9% and 52.1% for sandblasted-only and CNT-enhanced specimens, respectively.

3.5. Full-field strain analysis

The full-field axial strain evolution (in y direction) of the CNT-enhanced specimen at impact energy of 20 J is presented in Fig. 8(a) sorted by different loading time ratios t/T at a stationary legend. It can be seen that due to the deformation of impact dent, the axial strain in the titanium layer at the impacted side is redistributed under the tensile loading, and a significant stress concentration phenomenon appears on both sides of the dent. Fig. 8(b) presents the axial strain history along the final fracture path related to Fig. 8(a). The distance between the two peaks of its axial strain from the beginning of loading to fracture tends to decrease gradually, which is caused by the shallowing of dent depth under tensile loading. Relative to the intact specimen, the increment of axial strain along the fracture path with loading time is non-uniform for impacted specimens, which have the fastest strain growth rate on both sides of the dent compared to the edges of the laminate.

The axial strain nephogram of CNT-enhanced specimens at different impact energy levels for a loading time of 35 s is illustrated in Fig. 9(a). It can be observed that, with the same overall axial strain in the laminate, the local axial strain at both sides of the dent becomes more concentrated as the impact energy increases. As presented in Fig. 9(b) and (c), the axial strain of intact specimens is uniformly distributed along the fracture path, while for the impacted laminates, with increasing the impact energy, the axial strain increases and the peaks gradually move from the center to both sides of the dent. Additionally, in combination with the global dent depth, it can be determined that when the dent depth is greater than the half of laminate thickness, the strain peaks gradually move away from the center of the dent as the depth increases. For the cases with dent depth that less than the half of laminate thickness (3, 5 J for sandblasted-only specimens and 3, 5, 10 J for CNT-enhanced specimens), the strain peaks on both sides of the dent is not evident compared with the axial strain inside the dent. Besides, the strain peaks of sandblasted-only specimens along the fracture path are greater than that of CNT-enhanced cases with the same impact energy, which indicates a stronger susceptibility to failure for sandblasted-only laminates.

3.6. Analysis of fracture morphology

The tensile fracture morphology of the CNT-enhanced specimen after being subjected to impact energy of 20 J is shown in Fig. 10(a), which can be observed that the specimen still maintains a strong interfacial bonding ability after fracture, with delamination only at the initial impacted position. A large amount of fractured carbon fibers remains on

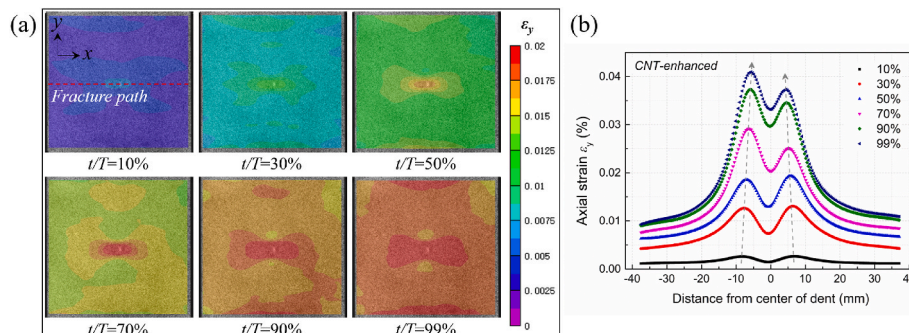


Fig. 8. For CNT-enhanced specimen subjected to impact energy of 20 J: (a) axial strain nephogram; (b) axial strain history along the fracture path.

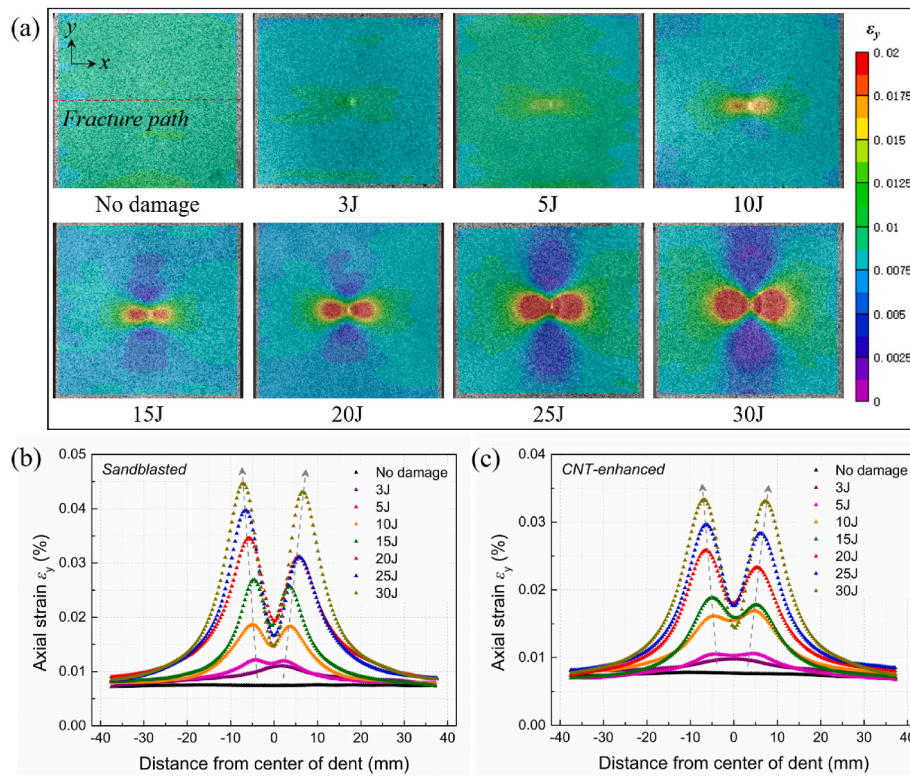


Fig. 9. For different impact energy levels at a loading time of 35 s: (a) the axial strain nephogram of CNT-enhanced specimens; the axial strain distributions of (b) sandblasted-only and (c) CNT-enhanced specimens along the fracture path.

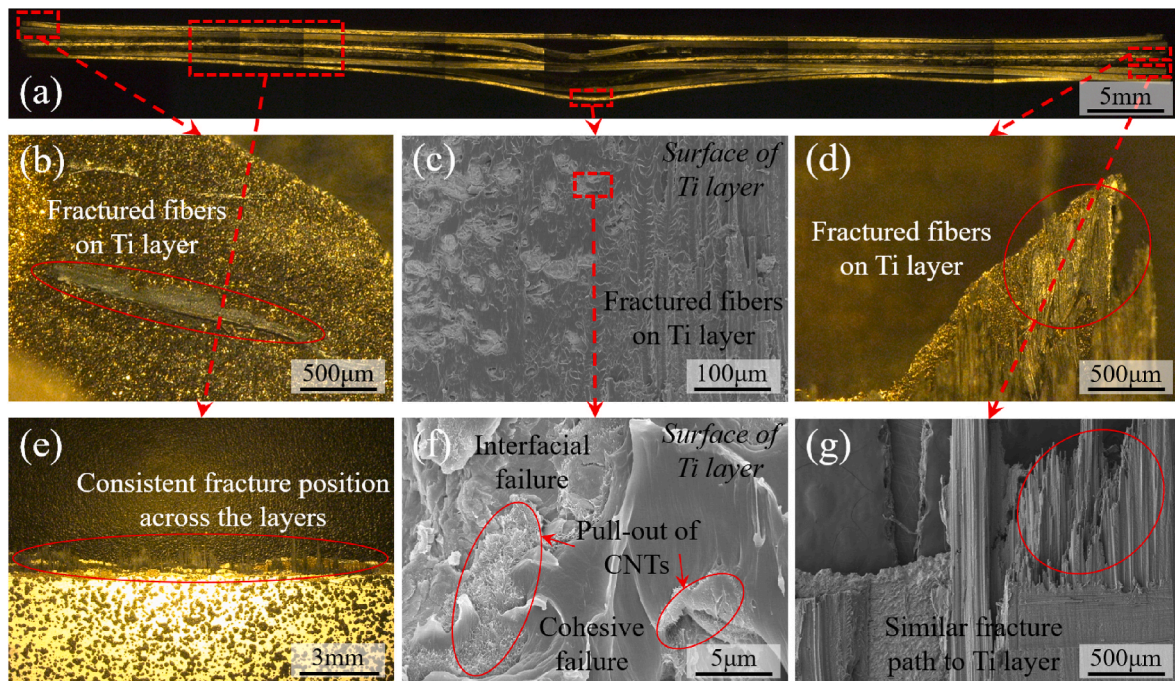


Fig. 10. Tensile fracture morphology of CNT-enhanced laminate at impact energy of 20 J.

the surface of the titanium layer as presented in Fig. 10(b–d), indicating an excellent interfacial adhesion between the metal and composites after the introduction of the CNT network structure. Besides, the impact causes mixed-mode delamination including interfacial and cohesive failures at the metal-composite interface, and forms a ductile fracture of PEEK, as shown in Fig. 10(f), where the PEEK is locked to the surface of

the titanium layer by CNT network structure and extensive pull-outs of CNTs occur locally. Moreover, compared with the fractures in the published literature [27], the good interfacial behavior within the laminates ensures that the fracture position is consistent across the layers as exhibited in Fig. 10(e), rather than being completely delaminated or fractured at different positions for different layers. It also demonstrates

that the components within the laminate do not experience layer-to-layer sliding under uniaxial tensile loading, whereby the displacement and strain are continuous at the metal-composite interface. In addition, Fig. 10(g) shows the adjacent composite layers of the titanium layer in Fig. 10(b), which has a similar fracture path to the shear deformation failure zone of the titanium at the edge of the laminate.

4. Theoretical prediction model of RTS considering internal thermal stress based on DIC data

4.1. Determination of internal thermal stress

Internal thermal stress is one of the important factors affecting the mechanical behaviors of FMLs [18]. In this study, the high-temperature cured thermoplastic resin PEEK was chosen as the matrix of the composite layers, which has an ideal curing temperature of 380–390 °C. As the significant difference in coefficients of thermal expansion (CTE) between titanium and CF/PEEK layers, the residual interlaminar thermal stress within the hybrid laminate manufactured by the hot-pressing method is bound to exist. Therefore, the residual thermal stresses within each layer of the hybrid laminate need to be considered when developing the ultimate strength prediction. For determining the thermal stress distribution within the CF/PEEK-titanium hybrid laminate, the classical laminated theory (CLT) was used to estimate the CTE of the laminate. According to the CLT, for a general asymmetric laminate without external mechanical loading, the thermal force resultant $\{N^{th}\}$ and thermal moment resultant $\{M^{th}\}$ generated by the temperature variation are related to the mid-plane strain $\{\epsilon^0\}$ and curvature $\{\kappa\}$ as

$$\begin{Bmatrix} N^{th} \\ M^{th} \end{Bmatrix} = \begin{bmatrix} A & B \\ B & D \end{bmatrix} \begin{Bmatrix} \epsilon^0 \\ \kappa \end{Bmatrix} \quad (1)$$

where, $[A]$, $[B]$, and $[D]$ are the extensional stiffness matrix, the bending-extension coupling stiffness matrix, and the bending stiffness matrix of the hybrid laminate, respectively, which are defined by

$$[A] = \sum_{k=1}^n [Q]_k (z_k - z_{k-1}) \quad (2)$$

$$[B] = \frac{1}{2} \sum_{k=1}^n [Q]_k (z_k^2 - z_{k-1}^2) \quad (3)$$

$$[D] = \frac{1}{3} \sum_{k=1}^n [Q]_k (z_k^3 - z_{k-1}^3) \quad (4)$$

where, $[Q]_k$ is the transformed reduced stiffness matrix for the k th lamina, n is the total number of layers and z is the distance measured from the middle plane.

$$[Q]_k = \begin{bmatrix} \frac{E_{11}}{1 - \nu_{12}\nu_{21}} & \frac{\nu_{21}E_{11}}{1 - \nu_{12}\nu_{21}} & 0 \\ \frac{\nu_{21}E_{11}}{1 - \nu_{12}\nu_{21}} & \frac{E_{22}}{1 - \nu_{12}\nu_{21}} & 0 \\ 0 & 0 & G_{12} \end{bmatrix}_k \quad (5)$$

Since the stacking sequence investigated in this study is an orthogonal anisotropic symmetric structure, the coupling stiffness matrix $[B]$ and thermal moment equal to 0 for the non-impacted case. Then, the thermal force resultant within the laminate as the temperature rises from ambient temperature to curing temperature can be expressed as

$$\{N^{th}\} = \Delta T \cdot \sum_{k=1}^n [Q]_k (z_k - z_{k-1}) \{\alpha\}_k \quad (6)$$

$$\Delta T = T_{cure} - T_{room} \quad (7)$$

It is assumed that no delamination appears within the laminate in the process of curing and cooling, and the layers shrink with equal strain during the cooling. The relation between CTEs of each component and the laminate can be obtained as Eq. (8) from the equilibrium of the thermal force resultant across the laminate.

$$\sum_{k=1}^n [Q]_k (z_k - z_{k-1}) (\{\alpha\}_k - \{\alpha\}_{lam}) = 0 \quad (8)$$

where, $\{\alpha\}_k$ and $\{\alpha\}_{lam}$ are the CTEs of the k th lamina and the laminate, respectively. Furthermore, the CTE of the laminate at laminate coordinate (x, y) can be determined by the CTEs of each component as Eq. (9) by transforming the above equations.

$$\{\alpha\}_{lam} = \begin{Bmatrix} \alpha_x \\ \alpha_y \\ \alpha_{xy} \end{Bmatrix}_{lam} = [A]^{-1} \cdot \sum_{k=1}^n [Q]_k (z_k - z_{k-1}) \begin{Bmatrix} \alpha_x \\ \alpha_y \\ \alpha_{xy} \end{Bmatrix}_k \quad (9)$$

Then the internal thermal stress of the k th layer $\{\sigma^{th}\}_k$ can be derived with

$$\{\sigma^{th}\}_k = [Q]_k (\{\alpha\}_k - \{\alpha\}_{lam}) \cdot \Delta T = [Q]_k \cdot \{\epsilon^{th}\}_k \quad (10)$$

Alternatively, the strain induced by the internal thermal stress in each component can be defined as the residual thermal strain $\{\epsilon^{th}\}_k$ to be convenient for subsequent calculations. Furthermore, for the post-impact specimens, out-of-plane deformation was generated at the dent, causing a deflection of the actual centerline relative to that of the intact laminate as illustrated in Fig. 11(a). In this case, the impacted specimen is not symmetric along the initial z -axis with respect to the intact state, hence the coupling stiffness matrix is no longer equal to 0, although the stacking sequence is orthogonally symmetric. Besides, it can be observed from Fig. 11(b) that there is an initial curvature around the dent, thus the effect of the initial curvature on the axial strain should be considered. As illustrated in Fig. 11(c), the dent created by the impact can be regarded as a hyperbolic structure, with R_1 and R_2 as the radius of curvature in the x and y directions, respectively. From the test results in Section 3.5, the maximum strain on the surface of laminate appears on both sides of the dent. By comparing with the transverse curvature at the same positions, it can be observed that these two points correspond to the minimum transverse curvature as shown in Fig. 11(d). Therefore, the RTS of the impacted laminate can be predicted analytically by establishing the constitutive model at the point with maximum initial axial strain.

In addition, impact damage such as fiber breakage, fracture in resin and metal can lead to a localized relaxation of internal thermal stress within the hybrid laminate. Accordingly, the initial internal thermal stress state needs to be determined for different damage conditions. With the results of damage assessment in Fig. 5(b), for impact energy in the range of 3–15 J, the damage is mainly dominated by local delamination of the metal-composite interface, without obvious fiber fracture, which implies that the plies are still subjected to the same initial internal thermal stresses as the intact laminate. With increasing impact energy, the fractures of the titanium layer, adhesive layer, CF/PEEK layers in 90° orientation, and in 0° orientation gradually appear on the non-impacted side of the laminate. For impact energy of 20–30 J, only the internal thermal stresses carried by the non-fracture layers need to be taken into account. Besides, when a layer is fractured during tensile loading, the internal thermal stresses will be redistributed simultaneously for achieving a new equilibrium of force resultants, which requires re-determination of the residual thermal stress within each layer (considering the transformed reduced stiffness matrix of the fractured layers is 0).

By considering the thermal strain generated by internal thermal stress as a virtual strain $\{\epsilon^{th}\}_k$, the stress-strain relation for the k th layer, and the relation between the global stress of the laminate and the stress of each layer according to the CLT can be obtained as

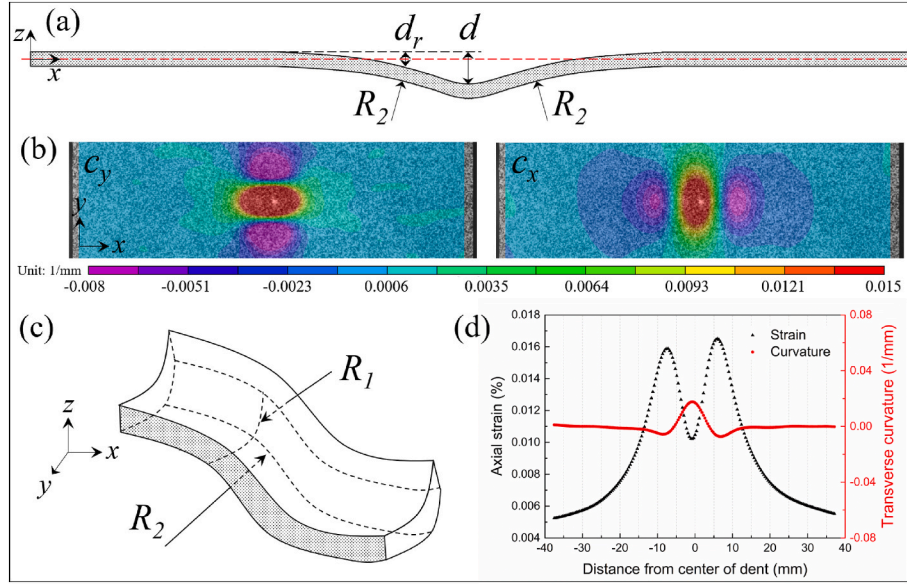


Fig. 11. (a) Cross-sectional schematic of the impacted specimen; (b) full-field axial and transverse curvature distributions of the CNT-enhanced specimen at the impact energy of 20 J; (c) schematic of the dent; (d) comparison of axial strain (in y direction) and transverse curvature (in x direction) along the fracture path.

$$\begin{Bmatrix} \sigma_{xx} \\ \sigma_{yy} \\ \tau_{xy} \end{Bmatrix}_k = [\mathbf{Q}]_k \begin{Bmatrix} \varepsilon_{xx} \\ \varepsilon_{yy} \\ \gamma_{xy} \end{Bmatrix}_k = [\mathbf{Q}]_k \left(\begin{Bmatrix} \varepsilon_{xx}^0 \\ \varepsilon_{yy}^0 \\ \gamma_{xy}^0 \end{Bmatrix} + z \begin{Bmatrix} \kappa_{xx} \\ \kappa_{yy} \\ \kappa_{xy} \end{Bmatrix} - \begin{Bmatrix} \varepsilon_{xx}^{th} \\ \varepsilon_{yy}^{th} \\ \gamma_{xy}^{th} \end{Bmatrix} \right) \quad (11)$$

$$\begin{Bmatrix} \sigma_{xx} \\ \sigma_{yy} \\ \tau_{xy} \end{Bmatrix}_{lum} = \sum_{k=1}^n \frac{z_k - z_{k-1}}{z_n - z_0} \begin{Bmatrix} \sigma_{xx} \\ \sigma_{yy} \\ \tau_{xy} \end{Bmatrix}_k \quad (12)$$

The force and moment resultants for the intact specimen in terms of laminate stiffnesses can be characterized as

$$\begin{Bmatrix} N \\ M \end{Bmatrix} = \begin{Bmatrix} N^m \\ M^m \end{Bmatrix} - \begin{Bmatrix} N^{th} \\ M^{th} \end{Bmatrix} = \begin{bmatrix} A & B \\ B & D \end{bmatrix} \begin{Bmatrix} \varepsilon^0 \\ \kappa \end{Bmatrix} - \begin{Bmatrix} N^{th} \\ M^{th} \end{Bmatrix} \quad (13)$$

For the cases with an impact dent, assuming that the thickness of each ply remains constant before and after the impact. According to the classical laminated shell theory (CLST) [36], the force and moment resultants for a given mechanical loading can be expressed as

$$\begin{aligned} \{N^m\} &= \begin{Bmatrix} N_{xx}^m \\ N_{yy}^m \\ N_{xy}^m \end{Bmatrix} = \sum_{k=1}^n \int_{z_{k-1}}^{z_k} \begin{Bmatrix} \sigma_{xx} \left(1 + \frac{z}{R_2}\right) \\ \sigma_{yy} \left(1 + \frac{z}{R_1}\right) \\ \tau_{xy} \left(1 + \frac{z}{R_2}\right) \end{Bmatrix} dz = \sum_{k=1}^n \int_{z_{k-1}}^{z_k} [\mathbf{Q}]_k \begin{Bmatrix} \varepsilon_{xx}^0 \left(1 + \frac{z}{R_2}\right) \\ \varepsilon_{yy}^0 \left(1 + \frac{z}{R_1}\right) \\ \gamma_{xy}^0 \left(1 + \frac{z}{R_2}\right) \end{Bmatrix} dz \\ &+ \sum_{k=1}^n \int_{z_{k-1}}^{z_k} z [\mathbf{Q}]_k \begin{Bmatrix} \kappa_{xx} \left(1 + \frac{z}{R_2}\right) \\ \kappa_{yy} \left(1 + \frac{z}{R_1}\right) \\ \kappa_{xy} \left(1 + \frac{z}{R_2}\right) \end{Bmatrix} dz \end{aligned} \quad (14)$$

$$\begin{aligned} \{M^m\} &= \begin{Bmatrix} M_{xx}^m \\ M_{yy}^m \\ M_{xy}^m \end{Bmatrix} = \sum_{k=1}^n \int_{z_{k-1}}^{z_k} z \begin{Bmatrix} \sigma_{xx} \left(1 + \frac{z}{R_2}\right) \\ \sigma_{yy} \left(1 + \frac{z}{R_1}\right) \\ \tau_{xy} \left(1 + \frac{z}{R_2}\right) \end{Bmatrix} dz \\ &= \sum_{k=1}^n \int_{z_{k-1}}^{z_k} z [\mathbf{Q}]_k \begin{Bmatrix} \varepsilon_{xx}^0 \left(1 + \frac{z}{R_2}\right) \\ \varepsilon_{yy}^0 \left(1 + \frac{z}{R_1}\right) \\ \gamma_{xy}^0 \left(1 + \frac{z}{R_2}\right) \end{Bmatrix} dz \\ &+ \sum_{k=1}^n \int_{z_{k-1}}^{z_k} z^2 [\mathbf{Q}]_k \begin{Bmatrix} \kappa_{xx} \left(1 + \frac{z}{R_2}\right) \\ \kappa_{yy} \left(1 + \frac{z}{R_1}\right) \\ \kappa_{xy} \left(1 + \frac{z}{R_2}\right) \end{Bmatrix} dz \end{aligned} \quad (15)$$

On simplification of the above equations using Eqs. (2)–(4), the expressions for the force and moment resultants with mid-plane strain and curvature induced by external mechanical loadings are

$$\{N^m\} = \begin{Bmatrix} N_{xx}^m \\ N_{yy}^m \\ N_{xy}^m \end{Bmatrix} = [\mathbf{A}] \begin{Bmatrix} \varepsilon_{xx}^0 \\ \varepsilon_{yy}^0 \\ \gamma_{xy}^0 \end{Bmatrix} + [\mathbf{B}] \begin{Bmatrix} \varepsilon_{xx}^0 \\ \varepsilon_{yy}^0 \\ \gamma_{xy}^0 \end{Bmatrix} + [\mathbf{B}] \begin{Bmatrix} \kappa_{xx} \\ \kappa_{yy} \\ \kappa_{xy} \end{Bmatrix} + [\mathbf{D}] \begin{Bmatrix} \kappa_{xx} \\ \kappa_{yy} \\ \kappa_{xy} \end{Bmatrix} \quad (16)$$

$$\{M^m\} = \begin{Bmatrix} M_{xx}^m \\ M_{yy}^m \\ M_{xy}^m \end{Bmatrix} = [B] \begin{Bmatrix} \epsilon_{xx}^0 \\ \epsilon_{yy}^0 \\ \gamma_{xy}^0 \end{Bmatrix} + [D] \begin{Bmatrix} \frac{\epsilon_{xx}^0}{R_2} \\ \frac{\epsilon_{yy}^0}{R_1} \\ \frac{\gamma_{xy}^0}{R_2} \end{Bmatrix} + [D] \begin{Bmatrix} \kappa_{xx} \\ \kappa_{yy} \\ \kappa_{xy} \end{Bmatrix} + [F] \begin{Bmatrix} \frac{\kappa_{xx}}{R_2} \\ \frac{\kappa_{yy}}{R_1} \\ \frac{\kappa_{xy}}{R_2} \end{Bmatrix} \quad (17)$$

where,

$$[F] = \frac{1}{4} \sum_{k=1}^n [Q]_k (z_k^4 - z_{k-1}^4) \quad (18)$$

Then, with consideration of internal thermal stress, the relation between the force and moment resultants of the laminate after impact and the mid-plane strain and curvature can be obtained as

$$\begin{Bmatrix} N \\ M \end{Bmatrix} = \begin{Bmatrix} N^m \\ M^m \end{Bmatrix} - \begin{Bmatrix} N^{th} \\ M^{th} \end{Bmatrix} = \begin{bmatrix} A + \frac{1}{R_m}B & B + \frac{1}{R_m}D \\ B + \frac{1}{R_m}D & D + \frac{1}{R_m}F \end{bmatrix} \begin{Bmatrix} \epsilon^0 \\ \kappa \end{Bmatrix} - \begin{Bmatrix} N^{th} \\ M^{th} \end{Bmatrix} \quad (19)$$

where, R_m represents R_1 or R_2 depending on the loading direction. In the case of uniaxial tensile loading where only N_{xx} is not zero, substituting the position of each layer in z -coordinate, the midplane strains, and curvatures into Eqs. (11) and (12) yields the stress-strain relationship for

the laminate with an impact dent considering the effect of internal thermal stress. In addition, the RTS of the laminate after impact can be obtained by substituting the radius of curvature at the maximum axial strain on the surface of the specimen. In particular, when R_m tends to infinity, the result corresponds to the case without impact dent.

The shape information on the impact dent without external loading (one representative specimen for each impact energy level) can be obtained from the DIC data as presented in Fig. 12(a–f). It can be seen that as the impact energy increases, the axial curvature gradually increases, while the transverse curvature and off-axis position corresponding to the maximum point of axial strain gradually decrease. As analyzed previously in Section 3.3, the global dent depth of the CNT-enhanced specimens is smaller than that of the sandblasted-only cases, for which similar rules are also applicable to their axial and transverse curvatures. The maximum off-axis position for both specimens is smaller than the macroscopically measured global dent depth because the white painting is prone to flow to the deepest part of the dent during the preparation of the speckles. However, it does not affect the acquisition of the z value corresponding to the maximum point of axial strain.

4.2. Constitutive modeling for the components in CF/PEEK hybrid laminate

For the titanium layer, two models should be applied for describing the constitutive behavior in its elastic and plastic regions, referring to Hooke’s law and the power-hardening law based on Ramberg-Osgood

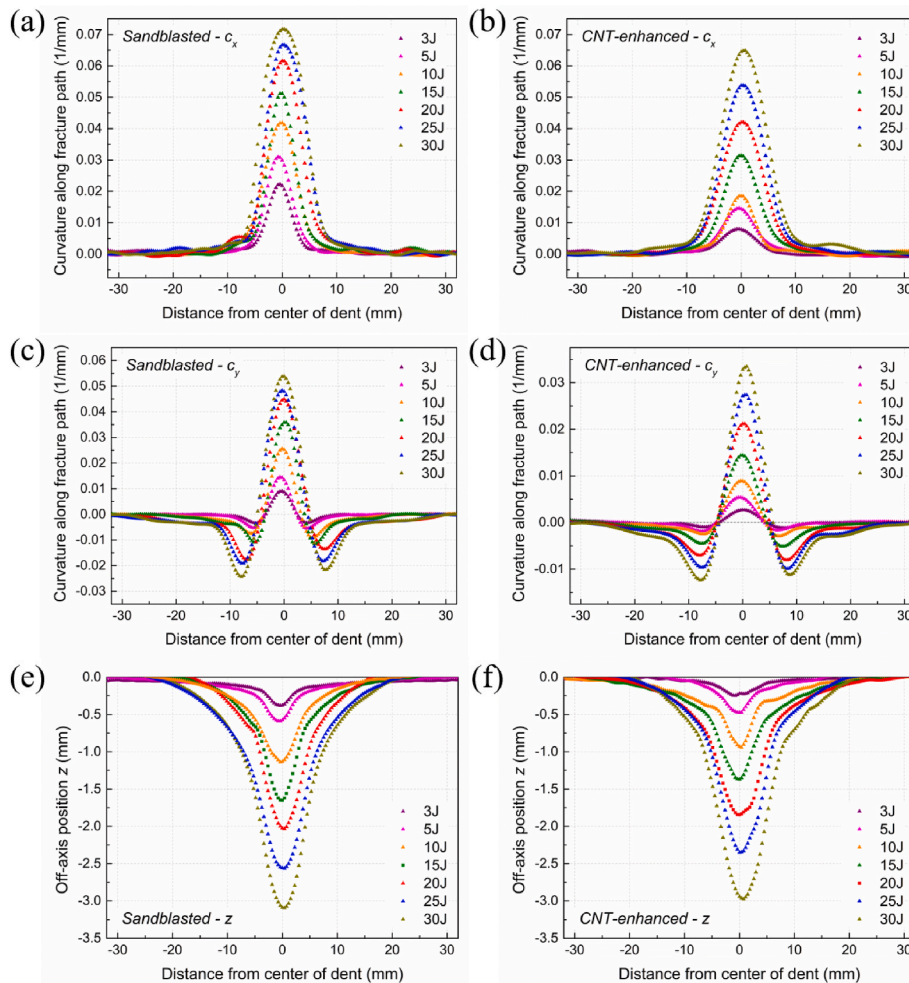


Fig. 12. Shape information on the impact dent at different impact energy levels: (a) Axial curvature, (c) transverse curvature and (e) off-axis position of sandblasted-specimens along the fracture path; (b) axial curvature, (d) transverse curvature and (f) off-axis position of CNT-enhanced specimens along the fracture path.

relation [37], respectively. Since the RTS under uniaxial tensile loading is investigated, the elastic-plastic model for the titanium layer can be established as

$$\sigma_{Ti} = \begin{cases} E_{11}^{Ti} \cdot \varepsilon_{xx,lam} & (\varepsilon_{xx,lam} \leq \varepsilon_p) \\ C \cdot (\varepsilon_{xx,lam})^n & (\varepsilon_{xx,lam} > \varepsilon_p) \end{cases} \quad (20)$$

where, C and n are material constants determined experimentally, which are 391.2 and 0.07, respectively. ε_p is the strain corresponding to the yield strength. A comparison of the stress-strain curve from the experiment and the proposed elastoplastic behavior is shown in Fig. 13.

Taking into account the effect of the internal thermal stress, the axial internal thermal strain can be equivalent to the material subjected to an axial virtual strain $\varepsilon_{xx,Ti}^{th}$, then the stress-strain relationship of titanium can be modified to obtain its thermomechanical response, which becomes

$$\sigma_{Ti} = \begin{cases} E_{11}^{Ti} \cdot (\varepsilon_{xx,lam} + \varepsilon_{xx,Ti}^{th}) & (\varepsilon_{xx,lam} + \varepsilon_{xx,Ti}^{th} \leq \varepsilon_p) \\ C \cdot (\varepsilon_{xx,lam} + \varepsilon_{xx,Ti}^{th})^n & (\varepsilon_{xx,lam} + \varepsilon_{xx,Ti}^{th} > \varepsilon_p) \end{cases} \quad (21)$$

For CF/PEEK and PEEK layers, the linear elastic model is used to describe the constitutive behavior according to Hooke's law, which can be expressed as

$$\{\sigma\}_{CF/PEEK} = [Q]_{CF/PEEK} \cdot \{\varepsilon\}_{lam} \quad (22)$$

$$\{\sigma\}_{PEEK} = [Q]_{PEEK} \cdot \{\varepsilon\}_{lam} \quad (23)$$

Since the plastic deformation of PEEK has a weak impact on the ultimate strength of the laminate [38], the effect attributed to its plastic region is not considered in this study. The mass content of carbon nanotubes in the CNT-enhanced layer is about 0.9% according to Ref. [29], and the direction of carbon nanotubes is randomly distributed during deposition. Therefore, it is considered that the CNT-enhanced layer only enhances the bonding behavior and has a limited effect on its tensile strength. From the analysis of Section 3, it is clear that the CNT-enhanced layer mainly influences the initial threshold of the laminate in delamination force, as well as the global dent depth after impact and the radius of curvature at the point of maximum axial strain. Similar to the titanium layer, the constitutive behaviors of CF/PEEK and PEEK layers by considering the internal thermal stress become

$$\{\sigma\}_{CF/PEEK} = [Q]_{CF/PEEK} \cdot (\{\varepsilon\}_{lam} + \{\varepsilon^{th}\}_{CF/PEEK}) \quad (24)$$

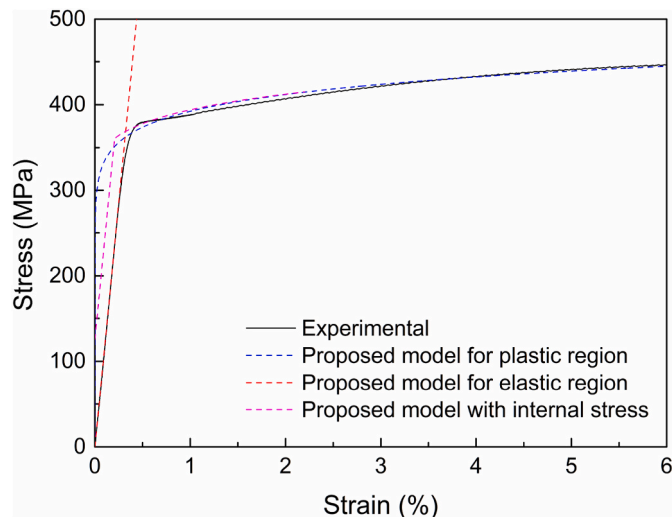


Fig. 13. Experimental and proposed elastoplastic behavior of titanium.

$$\{\sigma\}_{PEEK} = [Q]_{PEEK} \cdot (\{\varepsilon\}_{lam} + \{\varepsilon^{th}\}_{PEEK}) \quad (25)$$

4.3. Criterion of tensile failure

As the predicted post-impact RTS is obtained by applying a unidirectional loading to the specimen, regardless of the microscopic damage mechanism, then the maximum stress failure criterion is used for determining the failure of the laminate. The stress distribution in each component under the laminate coordinate system (x, y) can be derived from Eq. (17), which can be further converted into the stress distribution under the principal axes of the material by employing a transformation matrix as

$$\begin{Bmatrix} \sigma_{11} \\ \sigma_{22} \\ \tau_{12} \end{Bmatrix}_k = [T] \begin{Bmatrix} \sigma_{xx} \\ \sigma_{yy} \\ \tau_{xy} \end{Bmatrix}_k \quad (26)$$

According to the maximum stress failure criterion, failure is determined when one of the stresses within a layer reaches its critical strength in the principal directions of the material, which is defined by

$$(\sigma_{11}^c)_{ult} \leq \sigma_{11} \leq (\sigma_{11}^t)_{ult} \quad (27)$$

$$(\sigma_{22}^c)_{ult} \leq \sigma_{22} \leq (\sigma_{22}^t)_{ult} \quad (28)$$

$$|\tau_{12}| \leq (\tau_{12})_{ult} \quad (29)$$

where, C and T represent the compressive and tensile loading, respectively.

After the first component reaches its ultimate stress, the stiffness of this layer is recorded as 0, then the thermal residual stress distribution within the laminate should be redetermined by Eqs. (1)-(10) and substituted into Eq. (19) to repeat the above calculation procedures until complete failure of the laminate. The stress-strain curves of titanium and 0°-direction carbon fiber layers within the CNT-enhanced laminate at 10 J impact energy is illustrated in Fig. 14. For titanium-based hybrid laminates where titanium itself has excellent ductility, following the fracture of the carbon fiber layers in 0° orientation, the residual titanium layers are usually still in the plastic stage. Therefore, the ultimate strength of intact and post-impact laminates is mainly determined by the 0°-direction carbon fiber layer on the impacted side.

4.4. Validation of theoretical results

For sandblasted-only cases, the theoretical (with the input

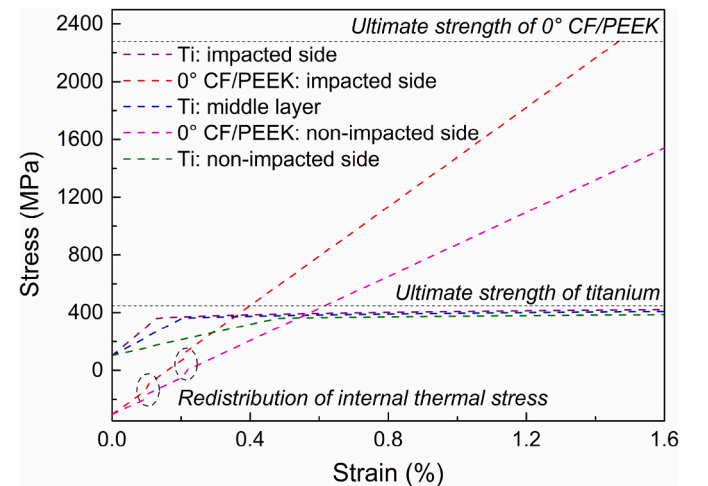


Fig. 14. Stress-strain curves of titanium and 0°-direction carbon fiber layers within the CNT-enhanced laminate at 10 J impact energy.

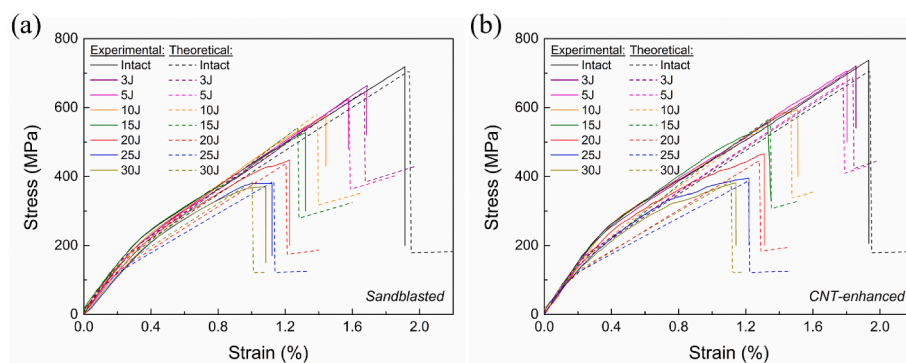


Fig. 15. Experimental and theoretical strain-stress curves: (a) for sandblasted-only specimens, (b) for CNT-enhanced specimens.

information from Fig. 12) and corresponding experimental strain-stress curves of intact and impacted specimens are shown in Fig. 15(a), the predictions at the RTS and failure strain are in good agreement with the experiments, with a maximum prediction error of 4% while 4.71% for the CNT-enhanced cases in Fig. 15(b), which may be attributed to the strengthening effect of the CNT layers that not being taken into account in the model. Moreover, it is noteworthy that, under low-energy impact conditions (3–15 J) with no fracture in each component, there is no need to consider the relaxation of the initial internal thermal stress, the developed model has a conservative prediction result on the stress-strain curve. After the fracture (20–25 J) occurs within the plies, the redistribution of initial thermal stress within each layer should be taken into account, which requires additional inspection for determination. Although the accuracy of the developed model is acceptable for the prediction of RTS and failure strain, the prediction of modulus degradation during loading is not satisfactory, therefore a more refined model is needed to divide the composite into more and thinner layers for calculation. Besides, it can be observed by comparing Fig. 15(a) and (b) that for the same initial internal thermal stress condition, the magnitude of initial curvature perpendicular to the loading direction and the local depth have a greater effect on the RTS at low-energy impacts (3–15 J) relative to the high-energy impacts (20–30 J), and the dent depth after high-energy impacts mainly affects the failure strain of the laminate and has little effect on its RTS. It can be concluded that the proposed unified analytical model could provide an acceptable prediction for the RTS and failure strain of the hybrid laminate after LVI under the consideration of internal thermal stress, for which the required parameters (including the off-axis position z , the axial and transverse radius of curvature) can be obtained simply by using the nondestructive testing technique such as DIC or a dent depth indicator. The proposed model can also be employed for FMLs with different layup structures and thicknesses of components to predict the post-impact tensile stress-strain relations, which can greatly reduce the experimental cost and provide a guidance for engineering applications.

It should be mentioned that the proposed model is based on the assumption that no delamination within the hybrid laminate appears. However, delamination is inevitable after impact that may lead to an increase in the local off-axis position z , which would further reduce the theoretically calculated RTS compared to the case without delamination. It can be observed from Fig. 5 that the delamination within hybrid laminate after impact mainly occurs at the interface between the titanium and the CF/PEEK layers inside dented area, and the increased off-axis position z acts primarily on the titanium layer at the non-impacted side. Besides, since the principal load-bearing component of the hybrid laminate is the carbon fiber layer in 0° orientation, when the carbon fiber layer reaches the failure strain, all the titanium layers at the maximum stress point have already entered into the plastic region as shown in Fig. 14, and the increase of the full-field strain makes little contribution to the stress increment within the titanium layer. Therefore, the delamination of the titanium layer within the dented area at the

non-impacted side has a limited effect on the theoretical RTS after impact. In this study, the cross-section of the impacted specimen is used to evaluate the initial fracture of metals and carbon fibers within the layers, which can be replaced by the detection methods such as C-scan or Micro-CT to achieve an ideal non-destructive prediction. In addition, the proposed model could be generalized to other series or stacking structures of FMLs (not limited in titanium-based) and the prediction of post-impact compression strength.

5. Conclusions

In summary, the low-velocity impact responses, damage mechanisms, and residual tensile behavior of sandblasted-only and CNT-enhanced CF/PEEK-Ti hybrid laminates were investigated. The results show that the initial delamination thresholds of force and displacement during impact can be significantly increased by interfacial enhancement of the CNT network. Besides, the inter-layered CNT network could suppress the deformation of the hybrid laminate, while a higher impact energy is required for the CNT-enhanced specimens to induce the same maximum permanent deformation. The delamination at the interface between the non-impacted side titanium and composite layers is the main failure mode for low-energy (3–15 J) impacts, which is dominated by fracture of fibers and metals for higher impact energy levels. In addition, it can be concluded from the experimental results of RTS that the CNT-enhanced laminate has a greater residual strength at the same impact energy. By using a 5% decrease in residual strength retention rate as a criterion for damage tolerance, a significant strength decrease starts to appear at 3 J for the sandblasted-only laminates, while it is improved to 10 J for the CNT-enhanced cases. Furthermore, the impact dent changes the distribution of strain on the surface of laminate under tensile loading, and the maximum axial strain is relocated at the position with maximum curvature of the dent. Moreover, the proposed unified constitutive model can provide an acceptable prediction for the residual ultimate strength and failure strain of the hybrid laminate after low-velocity impact under the consideration of internal thermal stress, for which the required parameters (including the off-axis position z , the axial and transverse radius of curvature) can be obtained simply by using the nondestructive testing technique such as DIC.

Declaration of competing interest

The authors declare that they have no known competing financial interests or personal relationships that could have appeared to influence the work reported in this paper.

Data availability

Data will be made available on request.

Acknowledgement

This work was financially supported by National Key Research and Development Program of China (2022YFB3707800), Science Foundation of the National Key Laboratory of Science and Technology on Advanced Composites in Special Environments, National Natural Science Foundation of China (Grant Number 11972008, 11972135), Heilongjiang Touyan Team (Grant Number HITTY-20190003) and China Scholarship Council (No. 202106120087). Besides, congratulations to Delft University of Technology on its 180th anniversary.

References

- [1] M.E. Kazemi, L. Shanmugam, S. Chen, L. Yang, J. Yang, Novel thermoplastic fiber metal laminates manufactured with an innovative acrylic resin at room temperature, *Compos Part A-Appl S* 138 (2020), 106043.
- [2] Y. Solyaev, A. Babaytsev, Direct observation of plastic shear strain concentration in the thick GLARE laminates under bending loading, *Compos. B Eng.* 224 (2021), 109145.
- [3] R. Alderliesten, Fatigue in fibre metal laminates: the interplay between fatigue in metals and fatigue in composites, *Fatig. Fract. Eng. Mater. Struct.* 42 (2019) 2414–2421.
- [4] R.M. Frizzell, C.T. McCarthy, M.A. McCarthy, An experimental investigation into the progression of damage in pin-loaded fibre metal laminates, *Compos. B Eng.* 39 (2008) 907–925.
- [5] G. Wu, J.-M. Yang, The mechanical behavior of GLARE laminates for aircraft structures, *JOM* 57 (1) (2005) 72–79.
- [6] D.A. Burianek, S.M. Spearing, Fatigue damage in titanium-graphite hybrid laminates, *Compos. Sci. Technol.* 62 (2002) 607–617.
- [7] Y.B. Hu, H.G. Li, L. Cai, J.P. Zhu, L. Pan, J. Xu, et al., Preparation and properties of Fibre–Metal Laminates based on carbon fibre reinforced PMR polyimide, *Compos. B Eng.* 69 (2015) 587–591.
- [8] C. Ji, J. Hu, B. Wang, Y. Zou, Y. Yang, Y. Sun, Mechanical behavior prediction of CF/PEEK-titanium hybrid laminates considering temperature effect by artificial neural network, *Compos. Struct.* (2020), 113367.
- [9] K. Dadej, J. Bienias, B. Surowska, On the effect of glass and carbon fiber hybridization in fiber metal laminates: analytical, numerical and experimental investigation, *Compos. Struct.* 220 (2019) 250–260.
- [10] L. Pan, Z. Zheng, A. Ali, Y. Lv, N. Roy, A. Zhang, et al., Evaluation of the parameters of titanium surface micro-pits on the titanium-PEEK joint fracture toughness, *Int. J. Adhesion Adhes.* 75 (2017) 165–173.
- [11] J. Ye, H. Wang, J. Dong, C. Liu, Y. Gao, B. Gong, et al., Metal surface nanopatterning for enhanced interfacial adhesion in fiber metal laminates, *Compos. Sci. Technol.* 205 (2021), 108651.
- [12] L. Shanmugam, M.E. Kazemi, Z. Rao, L. Yang, J. Yang, On the metal thermoplastic composite interface of Ti alloy/UHMWPE-Elium® laminates, *Compos. B Eng.* 181 (2020), 107578.
- [13] Y. Xu, H. Li, Y. Yang, Y. Hu, J. Tao, Determination of residual stresses in Ti/CFRP laminates after preparation using multiple methods, *Compos. Struct.* 210 (2019) 715–723.
- [14] M. Sadighi, R.C. Alderliesten, R. Benedictus, Impact resistance of fiber-metal laminates: a review, *Int. J. Impact Eng.* 49 (2012) 77–90.
- [15] C. Ji, B. Wang, J. Hu, Ca Zhang, Y. Sun, Effect of different preparation methods on mechanical behaviors of carbon fiber-reinforced PEEK-Titanium hybrid laminates, *Polym. Test.* 85 (2020), 106462.
- [16] H. Li, H. Wang, R. Alderliesten, J. Xiang, Y. Lin, Y. Xu, et al., The residual stress characteristics and mechanical behavior of shot peened fiber metal laminates based on the aluminium-lithium alloy, *Compos. Struct.* 254 (2020), 112858.
- [17] J. Hausmann, P. Naghipour, K. Schulze, Analytical and numerical residual stress models for fiber metal laminates - comparison and application, *Procedia Mater. Sci.* 2 (2013) 68–73.
- [18] S.U. Khan, R.C. Alderliesten, R. Benedictus, Post-stretching induced stress redistribution in Fibre Metal Laminates for increased fatigue crack growth resistance, *Compos. Sci. Technol.* 69 (2009) 396–405.
- [19] L. Shanmugam, M.E. Kazemi, C. Qiu, M. Rui, L. Yang, J. Yang, Influence of UHMWPE fiber and Ti6Al4V metal surface treatments on the low-velocity impact behavior of thermoplastic fiber metal laminates, *Adv. Compos. Hybrid Ma 3* (2020) 508–521.
- [20] Y. Lin, H. Li, Z. Zhang, J. Tao, Low-velocity impact resistance of Al/Gf/PP laminates with different interface performance, *Polymers* 13 (24) (2021) 4416.
- [21] X. Li, X. Zhang, H. Zhang, J. Yang, A.B. Nia, G.B. Chai, Mechanical behaviors of Ti/CFRP/Ti laminates with different surface treatments of titanium sheets, *Compos. Struct.* 163 (2017) 21–31.
- [22] P. Jakubczak, J. Bienias, M. Drozdziel, The collation of impact behaviour of titanium/carbon, aluminum/carbon and conventional carbon fibres laminates, *Thin-Walled Struct.* 155 (2020), 106952.
- [23] P. Jakubczak, The impact behaviour of hybrid titanium glass laminates- Experimental and numerical approach, *Int. J. Mech. Sci.* 159 (2019) 58–73.
- [24] R.C. Alderliesten, Designing for damage tolerance in aerospace: a hybrid material technology, *Mater. Des.* 66 (2015) 421–428.
- [25] P. Cortés, W.J. Cantwell, The prediction of tensile failure in titanium-based thermoplastic fibre–metal laminates, *Compos. Sci. Technol.* 66 (2006) 2306–2316.
- [26] K. Dadej, B. Surowska, J. Bienias, Isostrain elastoplastic model for prediction of static strength and fatigue life of fiber metal laminates, *Int. J. Fatig.* 110 (2018) 31–41.
- [27] A.P. Sharma, R. Velmurugan, Uni-axial tensile response and failure of glass fiber reinforced titanium laminates, *Thin-Walled Struct.* 154 (2020), 106859.
- [28] W.J.R. Christian, F.A. DiazDelaO, E.A. Patterson, Strain-based damage assessment for accurate residual strength prediction of impacted composite laminates, *Compos. Struct.* 184 (2018) 1215–1223.
- [29] C. Ji, J. Guo, J. Hu, B. Wang, Y. Sun, Enhanced interfacial adhesion of CF/PEEK-titanium hybrid laminates via introducing micro-nano layers with multi-walled carbon nanotube networks, *Compos. Sci. Technol.* 223 (2022), 109418.
- [30] J.R. Davis, *Metals Handbook Desk Edition*, ASM, 1998.
- [31] G.A. Schoepner, S. Abrate, Delamination threshold loads for low velocity impact on composite laminates, *Compos Part A-Appl S* 31 (2000) 903–915.
- [32] Y. Hu, X. Liu, F. Ji, J. Wei, W. Jiang, Y. Zhang, Effects of the electrophoretic deposition of CNTs on the mechanical properties of Ti/CFRP composite laminates, *ACS Omega* 7 (2022) 1337–1346.
- [33] T. Ouyang, R. Bao, W. Sun, Z. Guan, R. Tan, A fast and efficient numerical prediction of compression after impact (CAI) strength of composite laminates and structures, *Thin-Walled Struct.* 148 (2020), 106588.
- [34] A. Mahdian, J. Yousefi, M. Nazmdar, N.Z. Karimi, M. Ahmadi, G. Minak, Damage evaluation of laminated composites under low-velocity impact tests using acoustic emission method, *J. Compos. Mater.* 51 (2016) 479–490.
- [35] M. Damghani, N. Ersoy, M. Piorkowski, A. Murphy, Experimental evaluation of residual tensile strength of hybrid composite aerospace materials after low velocity impact, *Compos. B Eng.* 179 (2019), 107537.
- [36] M.K. Buragohain, *Composite Structures: Design, Mechanics, Analysis, Manufacturing, and Testing*, CRC press, 2017.
- [37] M.A. Meyers, K.K. Chawla, *Mechanical Behavior of Materials*, Cambridge university press, 2008.
- [38] L.-S. Wang, Z.-M. Huang, On strength prediction of laminated composites, *Compos. Sci. Technol.* 219 (2022), 109206.